Monte Carlo study of heat conductivity in stochastic boundaries: Application to the TEXTOR ergodic divertor

A. M. Runov and D. Reiter
Institut für Plasmaphysik, Forschungszentrum Jülich GmbH, EURATOM Association, Trilateral Euregio Cluster, D-52425 Jülich, Germany

S. V. Kasilov
Institute of Plasma Physics, National Science Center ''Kharkov Institute of Physics and Technology,'' 61108, Kharkov, Ukraine

M. F. Heyn and W. Kernbichler
Institut für Theoretische Physik, Technische Universität Graz, Petersgasse 16, A-8010 Graz, Austria

(Received 9 March 2000; accepted 7 December 2000)

The heat balance equation is derived and solved for fusion edge plasma conditions with (partially developed) ergodic magnetic-field structures. For this purpose, a three-dimensional (3D) Monte Carlo code, ''E3D,'' based upon the ''multiple local magnetic coordinate system approach'' has been developed. Parameters typical for the Dynamic Ergodic Divertor (DED) of TEXTOR-94 (Torus Experiment for the Technology Oriented Research) [K. H. Finken *et al.*, Fusion Eng. Des. **37**, 1 (1997)] are chosen in the applications. The plasma temperature fields and the profiles of the radial component of heat flux due to the classical parallel and anomalous perpendicular diffusion are calculated. Because of magnetic-field ergodization and diversion of field lines, parallel conduction also can contribute to this radial flux. The results are compared with theoretical predictions for two limiting cases: With the Rechester–Rosenbluth model of ergodization-induced transport and with a ''laminar flow model'' proposed in the present paper. This latter model describes the effects of field line diversion. The diversion effect is shown to be dominant for TEXTOR-DED conditions.

[DOI: 10.1063/1.1344921]

I. INTRODUCTION

External or intrinsic magnetic perturbations can provide a complex field topology in toroidal fusion edge plasmas, both in tokamaks and in stellarators. In these edge plasma regions ergodic, island, and ''laminar'' zones can coexist and, certainly, mutually influence each other in a complicated manner. Particle and energy transport in perturbed magnetic fields have been investigated theoretically for a long time (see, e.g., a review paper in Ref. 1).

If one uses an *ad hoc* ansatz for the anomalous transport normal to the field lines (e.g., Bohm-type diffusivities), transport phenomena can be quantified in two limiting cases: First, intact magnetic surfaces everywhere, and, second, in regions of fully developed ergodicity of the magnetic field.

In the first case, one introduces some ''global'' magnetic coordinate system,[2] aligned to magnetic surfaces. This choice avoids the otherwise numerically induced artificial cross-field transport due to mixing of parallel and perpendicular fluxes. This approach is very successful for geometrically ''regular'' toroidal systems like tokamaks[3] or stellarators[4] with, at the worst, regular chains of islands in the domain of integration.[5] Note that such a regular stellarator magnetic-field topology is only a particular case. Even in the same device ergodic layers may appear at the location of formerly regular islands, with increased plasma pressure.[6,7]

In the opposite limiting case (full ergodicity), one can employ stochastic arguments, e.g., the concept of magnetic-field diffusivity. This enables one to derive effective radial heat conduction (diffusion) coefficients. Such coefficients result from the combination of the intrinsic (anomalous) perpendicular transport and the contribution of the (classical) parallel transport fluxes, both having components in the radial direction.[8–11] The crucial prerequisite for such a treatment is the exponential divergence of two initially neighboring starting points, if one follows these points along their pertinent magnetic-field lines: $|\delta\mathbf{r}(l)| \propto |\delta\mathbf{r}_0| \exp(l/L_k)$. Here $|\delta\mathbf{r}|$ is the distance between the two points, l is the distance measured along the field lines, $\delta\mathbf{r}_0 = \delta\mathbf{r}(l=0)$, and L_k is a parameter (''Kolmogorov length''). It can be considered (quasi-linear theory) that this corresponds to a diffusive behavior of the field lines for large distances $l \gg L_k$, with $|\delta(l)| \approx \sqrt{2D_{\mathrm{fl}} l}$. Hence, under such conditions it is possible to parameterize the magnetic field in terms of a field line diffusion coefficient D_{fl} and a Kolmogorov length L_k (see Refs. 12 and 13).

Complementing these approaches there exist various approximate models[14–16] to describe the transport in the ''laminar zone,'' based upon ''lattice concepts.'' There is an ambiguity in the definition of the ''laminar flow zone'' in the literature. In the most simple approaches one defines the laminar zone as the region, where the distance from a material boundary to the next material boundary, measured along the field line (''connection length''), is well below the Kol-

mogorov length. The main idea of this approach is to precompute a (more or less representative) fixed set of magnetic-field lines and to employ some simplified (0D or 1D) transport treatment along these selected field lines. Although such reduced models can sometimes be quite useful for identifying the underlying physics (see Sec. IV C), they fail completely when statements of more quantitative nature are required. Indeed, the artificial separation of the region of interest into laminar and ''ergodic'' zones is questionable, since it is not clear *a priori* whether the boundary between them is a simply connected surface and, even if yes, which boundary conditions one should pose there? Furthemore, it has been shown in Ref. 17, that the attempt to use this latter concept directly for the entire region including both regular and ergodic zones leads to enormous numerical diffusion. This is because of the inherent but unphysical mixing of parallel and perpendicular transport by unavoidable reinterpolation on the Poincaré-sections, which is the basis of this procedure.

In more realistic situations, one has to deal with complex (intermediate) configurations where the ergodic, island and laminar zones are present simultaneously. Here, the ansatz of a diffusive behavior of the field lines is questionable.

If the magnetic field can be presented as a sum of an unperturbed background field with intact magnetic surfaces and a small perturbation field, the MHD equations can be solved with the help of spectral methods.[18–20] The convergence of these methods in the case of the heat balance equation has recently been demonstrated.[20]

There is another group of methods, which is less restricted with regard to the magnetic field topology. They are based upon ''mapping techniques.'' These methods were originally designed to model the dynamics of test particles[21,22] streaming along regular drift orbits in the presence of relatively weak diffusion in either physical or velocity space. In this approach, one introduces Poincaré sections which cut all orbits of interest. Then one treats the regular part of the motion using a known transformation of points from one section to the neighboring section (''mapping''). The diffusive processes are modeled by scattering of the particles in coordinate or velocity space on the Poincaré cut. With numerically pre-computed maps which are reconstructed using the ''interpolated cell mapping'' technique[23–25] and with properly defined collision operators as well as a proper choice of Poincaré cuts,[26,27] such a procedure becomes a rigorous method for solving the drift-kinetic equation.

The mapping technique is rather straightforward to introduce in the kinetic description when the ''parallel'' motion of the test particles between the cuts is convective. It is more intricate in the case of MHD equations, in particular the heat balance equation, where the parallel motion of ''test particles'' (more precisely: Heat elements) is essentially a diffusion process. Nevertheless, it is possible to define a mapping-based random walk process in parallel and perpendicular directions that satisfies the original MHD equation.[28,29]

In this paper we present a more advanced ''Multiple Coordinate System Approach'' (MCSA), in which the full trajectory of the fluid elements is now taken into account. The concept of mapping is still important here, as will be shown below (see Sec. III B). The main idea of using MCSA is based upon the fact, that the magnetic field lines can exhibit truly stochastic behavior only for large distances $l \gg L_k$, while for $l \leqslant L_k$, the field remains regular. This suggests that one can divide the computational domain into a finite set of sub-domains, each one with a typical field line length less than the Kolmogorov length. In each of these sub-domains we introduce separate so-called ''local'' magnetic coordinate systems. Such restricted coordinate systems can, for example, be obtained as a by-product when constructing Clebsch coordinates for open-ended systems, see Ref. 2.

Within a single sub-domain, a conventional Monte Carlo approach for parabolic equations in curvilinear coordinates (see Sec. III A) is used. If a fluid element crosses a boundary of a sub-domain, we use the ''interpolated cell mapping'' technique[23–25] to switch the coordinate system (see Sec. III B). In this ''Lagrangian'' concept, the individual fluid parcels retain their identity when they are handed over from one sub-domain to a neighboring sub-domain. This avoids the problems with numerical diffusion with Eulerian concepts encountered and identified in Ref. 17. The method permits to model plasma transport phenomena in magnetic fields of arbitrary structure, without any further geometrical idealization.

It should be emphasized that distinct from our earlier work,[29,30] where the parallel motion was described as a discrete process (test particles exist only on the Poincaré sections), the MCSA is based upon a continuous random walk process. Numerically, this provides a much better accuracy and geometrical flexibility of the algorithm.

The aim of the present paper is twofold. First, we derive a very general algorithm for solving diffusion-advection like equations in almost arbitrary magnetic geometry. Second, we apply it to the particular problem of heat transfer in the scrape-off layer of TEXTOR DED.[31]

The structure of the present paper is as follows. In Sec. II we derive the basic heat balance equation in tensor form for arbitrary curvilinear geometry. In Sec. III the Monte Carlo procedure for solving this equation, based upon MCSA, is described. In Sec. IV we apply this method to solve the heat transfer problem in the magnetic configurations produced by the dynamic ergodic divertor (DED) of TEXTOR. Here we take advantage of the unique capability of the microscopic resolution inherent to our Monte Carlo treatment of the fluid problem. We are able to separate fluxes Q in the radial direction by their physical origin: Into a flux $Q_\perp$ caused by anomalous cross-field diffusion and a radial flux $Q_\parallel$ originated by the magnetic field perturbation. This enables us to assess, quantitatively, the validity of theoretical predictions for heat transport in TEXTOR-DED under far less restrictive assumptions than hitherto possible.

II. BASIC EQUATION IN TENSOR FORM

In the present paper we treat only the effect of the perturbation field on the electron heat conduction, because this

quantity is most sensitive to the magnetic geometry. Because of the geometrical complications, we have to write electron heat balance equation in a proper coordinate system.

We start by recalling the heat balance equations for an electron-ion fluid in the following vector form of the conservation law [compare to Braginski's equations (1.23), Ref. 32]:

$$\frac{\partial u_\alpha}{\partial t}+\nabla\cdot\left[(\mathbf{V}_{\perp\alpha}+\mathbf{h}V_{\parallel\alpha})u_\alpha-\frac{2}{3}\chi_{\perp\alpha}\nabla u_\alpha\right.$$
$$\left.-\frac{2}{3}(\chi_{\parallel\alpha}-\chi_{\perp\alpha})\mathbf{hh}\cdot\nabla u_\alpha\right]=-\nu_\alpha u_\alpha+S_\alpha^{(u)}. \quad (1)$$

Here the subscript $\alpha=e,i$ stands for the sort of particles (electrons and ions), $u_\alpha\equiv 3nT_\alpha/2$ and T_α are the internal energy and temperature of the species α, respectively, n is the plasma density, $\mathbf{h}=\mathbf{B}/B$ is a unit vector along the magnetic field and

$$\mathbf{V}_{\perp\alpha}\equiv\left(1-\frac{2}{3}\frac{\chi_{\perp\alpha}}{D_\perp}\right)\mathbf{V}_\perp, \quad V_{\parallel\alpha}\equiv V_\parallel+\frac{2}{3}\frac{1}{n}\chi_{\parallel\alpha}\mathbf{h}\cdot\nabla n, \quad (2)$$

$$\chi_{\perp\alpha}\equiv\frac{\kappa_{\perp\alpha}}{n}, \quad \chi_{\parallel\alpha}\equiv\frac{\kappa_{\parallel\alpha}}{n}, \quad (3)$$

are the perpendicular and parallel velocities and heat diffusivities of respective particles, $\kappa_{\perp\alpha}$ and $\kappa_{\parallel\alpha}$ are the anomalous perpendicular and classical parallel thermal conductivity coefficients, $V_\parallel$ is the parallel fluid velocity and $\mathbf{V}_\perp$ is the perpendicular fluid velocity due to the anomalous particle diffusion with coefficient $D_\perp$. It is assumed that electrons have the same convection velocity as the ions and thus the electrical plasma currents are neglected. The heat loss rates ν_α are given by

$$\nu_\alpha\equiv\nu_{\alpha 0}+\tfrac{2}{3}\mathrm{div}\,\mathbf{V}+\nu_{ie}, \quad (4)$$

where $\nu_{\alpha 0}$ is the heat loss rate due to inelastic processes and ν_{ie} describes the Coulomb energy exchange between electrons and ions. Neglecting the viscous heating of the electron component we write the generalized heat sources $S_\alpha^{(u)}$ as

$$S_e^{(u)}\equiv S_{e0}^{(u)}+\nu_{ie}u_i, \quad S_i^{(u)}\equiv S_{i0}^{(u)}+\nu_{ie}u_e-\pi^{ij}\frac{\partial V_i}{\partial r^j}, \quad (5)$$

where $S_{\alpha 0}^{(u)}$ is the energy source due to inelastic processes and π^{ij} is the viscous stress tensor.

In general curvilinear coordinates x^i the heat balance equation (1), and also the continuity equation and parallel momentum conservation law can be written in form of a conservation law for a fluid property f

$$\frac{\partial f}{\partial t}=\frac{1}{\sqrt{g}}\frac{\partial}{\partial x^i}\sqrt{g}\left(D^{ij}\frac{\partial f}{\partial x^j}-V^i f\right)-\nu f+S^{(f)}. \quad (6)$$

Here, g is the metric determinant and D^{ij} is the diffusion tensor appropriate for f

$$D^{ij}=D_\perp g^{ij}+(D_\parallel-D_\perp)h^i h^j, \quad (7)$$

where $g^{ij}=(\nabla x^i)\cdot(\nabla x^j)$, $V^i=\mathbf{V}\cdot\nabla x^i$ and $h^i=\mathbf{h}\cdot\nabla x^i$ are contravariant components of the metric tensor, of the convection velocity and of the unit vector along the magnetic field, respectively. (We have omitted the subscript α on the components of the diffusion tensor and the fluid velocity.)

The fluid equation (6) describes both, the relaxation of plasma parameters along and across the magnetic field. In the fusion plasma parameter range these processes have quite different time scales; e.g., the ratio of perpendicular to parallel heat relaxation times is proportional to $\chi_\parallel/\chi_\perp$ and can be of the order of 10^7 for electrons. Therefore, for the numerical solution of Eq. (6) in systems with existing magnetic surfaces (these can include island magnetic surfaces as well, see Ref. 5) magnetic coordinates must be used. This is necessary to avoid the numerically induced artificial cross-field transport due to the mixing of parallel and perpendicular heat fluxes (problem is numerically ''stiff''). In our case, the magnetic field has a more complex topology. Together with regions of intact magnetic surfaces, it includes regions with magnetic islands and also layers with ergodic magnetic field structure. Let us construct a general class of possible coordinate systems, which would permit strict separation of perpendicular and parallel fluxes. Later (Sec. III B) we will then specialize to the particular set of coordinate systems used in the applications discussed in this paper. For such a coordinate system, the minimum requirement is that the first two variables x^i must satisfy the magnetic differential equation

$$\mathbf{h}\cdot\nabla x^i=0, \quad i=1,2, \quad (8)$$

while the third variable, x^3, is an angle-like variable which is increasing along the magnetic-field lines

$$\mathbf{h}\cdot\nabla x^3>0. \quad (9)$$

Hence we require that the covariant base vector $\mathbf{e}_3$ points along the magnetic-field line.

Note that, in particular, this is the type of coordinate systems that are used in fusion plasma analysis to construct magnetic stream functions (Clebsch coordinates[2]).

As a result of these constrains, in such coordinates the parallel flux has only one nonvanishing component. That can be seen, e.g., from the resulting form of the diffusion tensor (7)

$$D^{ij}=D_\perp g^{ij}+(D_\parallel-D_\perp)(h^3)^2\delta_3^i\delta_3^j, \quad (10)$$

where δ_k^i is a Kronecker symbol.

III. MONTE CARLO PROCEDURE

In this section we describe the principles of MCSA for a diffusion-advection equation like Eq. (6). As it has been pointed out above, we introduce a set of magnetic coordinate systems according to Eqs. (8) and (9), each one having finite range. We start by specifying the Monte Carlo procedure within one coordinate system (Sec. III A). The resulting algorithm will also be relevant for computational domains without any further subdivision into sub-domains with distinct local coordinate systems. In Sec. III B we introduce the subdivision of our computational domain and the set of local coordinate systems as used in our particular TEXTOR DED application. Then, we describe the technique of switching between the local coordinate systems by means of ''interpolated cell mapping.''

A. The general algorithm: One elementary time step

We employ the conventional Monte Carlo procedure consisting of simulation of random walks from a discontinuous Markoff-process. This process is chosen to approximate a diffusion process. The internal energy contained in the system, W, is distributed between an ensemble of N_p test particles, $W=N_p w$. Here w is the initial weight of a single test particle (by abuse of language; it is common to refer to test particles, even if they represent portions of mass, momentum or energy in a fluid representation). The whole plasma volume is sub-divided into cells that are small compared to the characteristic gradient length of the plasma parameters. Thus, the internal energy density averaged over a given cell is estimated as the sum of the weights of particles in this cell divided by the cell volume.

In order to derive the elementary time step we rewrite (6), with f specialized to the internal energy u, in a Fokker–Planck form for the pseudo-scalar density of fluid parcels $N=u\sqrt{g}/w$

$$\frac{\partial N}{\partial t}=\frac{\partial}{\partial x^i}\left[\frac{\partial}{\partial x^j}D^{ij}N-V_c^i N\right]-\nu N+S^{(N)}, \tag{11}$$

where

$$V_c^i=V^i+\frac{1}{\sqrt{g}}\frac{\partial}{\partial x^j}\sqrt{g}D^{ij}. \tag{12}$$

The source and sink terms $S^{(N)}=S^{(u)}\sqrt{g}/w$ and νN can be accounted for by weight adjustment in a straightforward Monte Carlo manner. They shall not be discussed further here. In the following we describe only the treatment of the dynamics of the test particles (heat elements). The random process governing the motion of a fluid element is

$$x^i(t+\Delta t)=x^i(t)+\Delta x^i, \tag{13}$$

where Δx^i are small random steps and $\Delta t \ll \tau_{\min}$. Here, $\tau_{\min}$ is the shortest relaxation time, typically corresponding to parallel relaxation $\tau_{\min}=\chi_\parallel/L_\parallel^2$, $L_\parallel$ is the parallel spatial scale of plasma and magnetic-field parameters. The Fokker–Planck equation for the density of fluid elements N subjected to random process (13) coincides with (11) if

$$\langle \Delta x^i \Delta x^j\rangle = 2D^{ij}(\mathbf{x}(t))\Delta t, \quad \langle \Delta x^i\rangle = V_c^i(\mathbf{x}(t))\Delta t, \tag{14}$$

where $\langle\cdots\rangle$ is the expectation value. The error in the distribution function computed from this random process is quadratic in Δt after one time step. Using any set of independent random numbers ξ_i which satisfies

$$\langle \xi_i\rangle = 0, \quad \langle \xi_i \xi_j\rangle = \delta_{ij}, \tag{15}$$

with δ_{ij} being the Kronecker symbol, the elementary step can be realized in the following form:

$$\Delta x^i=\sqrt{2\Delta t}\alpha^{ij}\xi_j+V_c^i(\mathbf{x}(t))\Delta t. \tag{16}$$

Here α^{ij} is a square-root matrix which satisfies

$$\alpha^{ik}\alpha^{jl}\delta_{kl}=D^{ij}(\mathbf{x}(t)). \tag{17}$$

The random process (16) satisfies (14) up to terms linear in Δt. Within this precision during one time step one can model separately different types of transport processes, namely the anomalous perpendicular diffusion and classical parallel diffusion, using independent sets of random numbers for each process

$$\Delta x^i=\Delta x_\perp^i+\Delta x_\parallel^i, \tag{18}$$

where

$$\Delta x_\perp^i=\sqrt{2\Delta t}\alpha_\perp^{ij}\xi_j+V_{\perp c}^i\Delta t, \tag{19}$$

$$\Delta x_\parallel^3=\sqrt{2\Delta t D_\parallel^{33}}\xi_3+V_{\parallel c}^3\Delta t, \tag{20}$$

and $\Delta x_\parallel^i=0$ for $i=1,2$. Here

$$\alpha_\perp^{11}=\sqrt{D_\perp^{11}}, \quad \alpha_\perp^{21}=\frac{D_\perp^{12}}{\alpha_\perp^{11}}, \quad \alpha_\perp^{22}=\sqrt{D_\perp^{22}-(\alpha_\perp^{21})^2},$$

$$\alpha_\perp^{31}=\frac{D_\perp^{13}}{\alpha_\perp^{11}}, \quad \alpha_\perp^{32}=\frac{D_\perp^{23}-\alpha_\perp^{21}\alpha_\perp^{31}}{\alpha_\perp^{22}}, \tag{21}$$

and the remaining components of matrix $\alpha_\perp^{ij}$ are zero. The rest of notation in (19)–(21) is as follows:

$$D_\perp^{ij}=D_{\perp e}[g^{ij}-(h^3)^2\delta_3^i\delta_3^j], \quad D_\parallel^{33}=D_{\parallel e}(h^3)^2, \tag{22}$$

$$V_{\perp c}^i=\mathbf{V}_{\perp e}\cdot\nabla x^i+\frac{1}{\sqrt{g}}\frac{\partial}{\partial x^j}\sqrt{g}D_\perp^{ij},$$

$$V_{\parallel c}^3=V_{\parallel e}h^3+\frac{1}{\sqrt{g}}\frac{\partial}{\partial x^3}\sqrt{g}D_\parallel^{33}, \tag{23}$$

where diffusion coefficients and convection velocities entering (22) and (23) are given by (2) and (3) for $\alpha=e$. Note that we have satisfied system (17) which contains, in general, six independent equations with only five quantities (21) because the tensor $D_\perp^{ij}$ is degenerate (perpendicular diffusion is zero along the field lines). For this reason only two random numbers, ξ_1 and ξ_2 are required in (19).

B. Multiple local magnetic coordinate systems

The coordinates x^i are constructed starting from some appropriate real-space coordinates. In our particular case these latter are quasi-toroidal coordinates (r,θ,φ) being the small radius (which may readily be generalized to a flux-surface label), poloidal and toroidal angles, respectively. First, one or several ''reference cuts'' (''Poincaré sections'') are introduced. These are surfaces which are nowhere tangent to the magnetic field lines in the computational domain (e.g., $\theta=$const in our example). Then, the coordinate lines on this cut (in our case: $r=$const and $\varphi=$const) are traced along the magnetic-field lines. The surfaces formed in this way from the coordinate lines $r=$const and $\varphi=$const are the coordinate surfaces $x^1=$const and $x^2=$const, respectively. Since these coordinate surfaces contain the magnetic-field lines, the coordinates x^1 and x^2 obviously satisfy the magnetic differential equation (8). The conditions that $x^1=r$ and $x^2=\varphi$ on the reference cut are the boundary conditions for (8).

For the magnetic fields in toroidal devices, solutions to the magnetic differential equation (8) are, generally, not

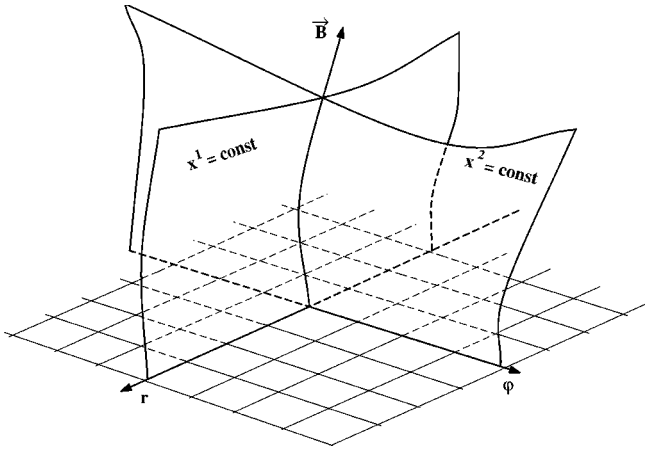

FIG. 1. Coordinate surfaces of local magnetic coordinates $x^1=x^1_{(m)}$ and $x^2=x^2_{(m)}$. Magnetic field-lines are given by intersections of these surfaces. At the reference cut x^1 and x^2 coincide with quasi-toroidal coordinates r and φ.

single-valued functions (after one revolution over θ the intersections of our coordinate surfaces with the reference cut will not coincide with original lines $r=\text{const}$, $\varphi=\text{const}$ anymore).

In the special case when nested magnetic surfaces exist, possible single valued solutions to (8) are functionally dependent. They can be expressed as functions of toroidal magnetic flux used as radial coordinate in flux coordinate systems.

In the more general case of interest here, and in order to obtain independent solutions of the magnetic differential equation (8) as coordinates, it is necessary, first, to use more than one reference cut, and, second, to introduce an additional set of surfaces which cut magnetic-field lines. These surfaces are periodicity boundaries limiting the domain where functions x^1 and x^2 are single valued. Thus, our magnetic coordinates x^1 and x^2 have a simple geometrical meaning: They are real space coordinates of the projection along the magnetic-field line of the observation point to the nearest reference cut (see Fig. 1).

Practically, a single reference cut is not sufficient to cut all the field lines of interest because of the presence of ''open'' field lines at the edge of the plasma volume. These wind around magnetic coils and form ''private flux regions'' in the computational domain. In addition, the coordinate system becomes strongly nonorthogonal and disordered far away from the reference cut, in case of strong ergodicity. Therefore, several reference cuts (and corresponding domain boundaries) are needed in the general case. As a consequence, in each of the regions separated by domain boundaries a ''private'' local magnetic coordinate system is constructed as described above from the ''Poincaré section'' (reference cut) belonging to that particular sub-domain (see Fig. 2).

Correspondingly, the cells for computation of the local plasma parameters introduced in the previous subsection are limited by the domain boundaries along the magnetic-field lines (see Fig. 3) and form a rectangular mesh over coordinates x^1 and x^2.

For the special case $((r,\theta,\varphi)$-system, reference cuts

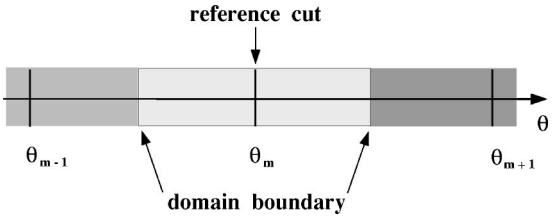

FIG. 2. Sub-domain of one local magnetic coordinate system. Coordinates are constructed from reference cut (Poincaré section). Transition to next local coordinate system at ''domain boundary.''

$\theta=\text{const}$) the formal solutions to the magnetic differential equation (8) are given by the characteristics $X^1(r,\varphi,\theta;\theta')$ and $X^2(r,\varphi,\theta;\theta')$ which satisfy the magnetic field line equations

$$\frac{\partial X^1}{\partial\theta'}=\frac{h^r(X^1,X^2,\theta')}{h^\theta(X^1,X^2,\theta')},\quad \frac{\partial X^2}{\partial\theta'}=\frac{h^\varphi(X^1,X^2,\theta')}{h^\theta(X^1,X^2,\theta')}, \tag{24}$$

and initial conditions

$$X^1(r,\varphi,\theta;\theta)=r,\quad X^2(r,\varphi,\theta;\theta)=\varphi. \tag{25}$$

Here $h^r(r,\varphi,\theta)$, $h^\varphi(r,\varphi,\theta)$ and $h^\theta(r,\varphi,\theta)$ are quasi-toroidal contravariant components of **h**. The reference cuts are introduced by

$$\theta=\theta_m,\quad \theta_m=\theta_0+m\Delta\theta,\quad \Delta\theta=\frac{2\pi}{M},\quad m=1,2,\ldots,M, \tag{26}$$

where $\theta_0=\text{const}$ and M is the total number of the reference cuts. The corresponding sets of local magnetic coordinates $x^i_{(m)}$ are defined with the help of the characteristics X^i as follows:

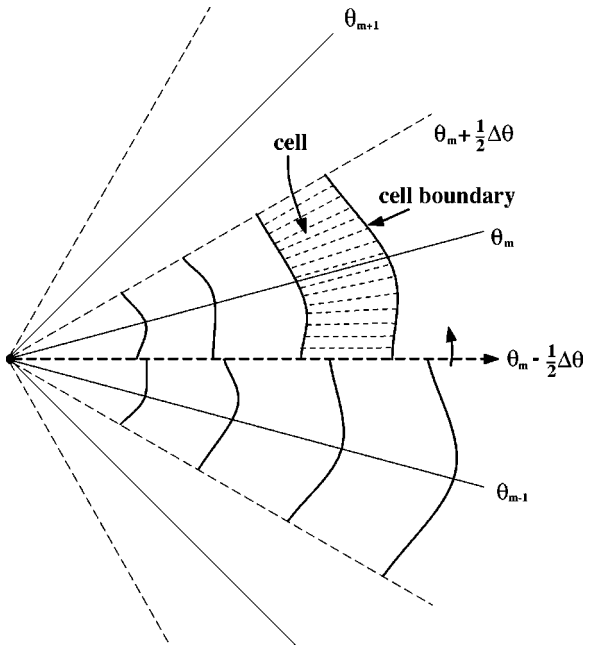

FIG. 3. Structure of cells for computing ''box-averaged'' internal energy density. The reference cut, $\theta=\theta_m$, and domain boundaries, $\theta=\theta_m+\Delta\theta/2$ and $\theta=\theta_m-\Delta\theta/2$ are also indicated.

$$x^i_{(m)} \equiv X^i(r,\varphi,\theta;\theta_m), \quad i=1,2, \quad x^3_{(m)} = \theta - \theta_m . \tag{27}$$

Using the group property of characteristics

$$X^i(X^1(r,\varphi,\theta;\theta''),X^2(r,\varphi,\theta;\theta''),\theta'';\theta') = X^i(r,\varphi,\theta;\theta'), \tag{28}$$

the inverse coordinate transformation is obtained

$$r = X^1(x^1_{(m)},x^2_{(m)},\theta_m;\theta), \quad \varphi = X^2(x^1_{(m)},x^2_{(m)},\theta_m;\theta), \quad \theta = \theta_m + x^3_{(m)} . \tag{29}$$

A schematic picture of coordinate surfaces is shown in Fig. 1. If a point described in the local coordinate system m used in the domain

$$\theta_m - \tfrac{1}{2}\Delta\theta < \theta < \theta_m + \tfrac{1}{2}\Delta\theta, \tag{30}$$

crosses one of the domain boundaries, the corresponding local coordinates in the neighboring coordinate system are obtained with help of (27), (29), and the group property (28)

$$\begin{aligned} x^i_{(m\pm1)} &\equiv X^i(r,\varphi,\theta;\theta_{m\pm1}) \\ &= X^i(x^1_{(m)},x^2_{(m)},\theta_m;\theta_{m\pm1}) \\ &\equiv X^i_{(\pm,m)}(x^1_{(m)},x^2_{(m)}), \quad i=1,2, \\ x^3_{(m\pm1)} &= x^3_{(m)} \mp \frac{2\pi}{M}. \end{aligned} \tag{31}$$

Functions $X^i_{(\pm,m)}$ define the Poincaré map of the magnetic field in positive $(+)$ and negative $(-)$ directions, respectively. Our reference cuts are the Poincaré sections for these maps. Since the particular set of local magnetic coordinates is used only in its own sub-domain, we omit subscript (m) on the coordinates and, instead, include it in the set of variables as an additional, discrete, variable, $\mathbf{x} \equiv (x^1,x^2,x^3,m)$.

The procedure of construction of local coordinate systems described above is rather general, e.g., one can use toroidal reference cuts $\varphi = \varphi_m$ and cylindrical coordinates R, Z, φ instead of quasi-toroidal coordinates. The corresponding formulas are obtained by the change $r,\varphi,\theta \to R,Z,\varphi$ in the notation.

In local magnetic coordinates the slow cross-field transport is clearly separated from the fast parallel transport. Therefore, the only source of numerical cross-field diffusion due to the stiffness of the problem can be at the transition of one local coordinate system to the next one (31). For this reason, functions (31) defining Poincaré maps which are precomputed using the numerical integration of the magnetic-field line equations (24) for a mesh of initial points are reconstructed with high accuracy using interpolation with bicubic splines, just as in the well established ''interpolated cell mapping'' procedure.[25] The accuracy requirements to the spline mesh are described in Appendix A.

C. Numerical realization

The computation with the code E3D is performed in two stages. At the first stage the geometrical parameters characterizing the magnetic configuration and wall geometry are pre-computed and stored. These include the values of mapping functions $X^i_{(\pm,m)}$ that define the mutual coordinate transforms between the neighboring local coordinate systems [see (31)]. They are obtained by numerical integration of the magnetic-field line equations (24). For a TEXTOR-DED simulation we use, typically, $M=20$ reference cuts with a grid 20×20 in x^1 and x^2 on each cut (''magnetic mesh''). Such a grid is consistent with the accuracy estimates in Appendix A.

In addition, we introduce a 3D ''parameter'' mesh consisting of cells for evaluation of plasma parameters from particle trajectories by means of box-averaging. On this mesh, we pre-compute and store those parameters of the metric tensors of all local magnetic coordinate systems which enter formulas (22) and (23). This parameter mesh does not need to be the same as the ''magnetic'' mesh because plasma parameters have a different spatial scale. Here we use, typically, a resolution of $40\times20\times20$ in (x^1,x^2,x^3), respectively.

Finally, we pre-compute the magnetic coordinates of all material boundaries of the problem as well as the inverse coordinate transform of the magnetic coordinates to real-space coordinates on the wall. The latter information is used, e.g., for the evaluation of flux- and power deposition patterns.

At a second stage we perform the transport modeling itself. At this stage the evolution of the initial distribution of internal energy u is followed until the stationary state is reached. Since transport coefficients are nonlinear functions of plasma parameters, these parameters are adjusted after the time intervals $\Delta t_r \ll \tau_r$, where τ_r is a typical profile relaxation time. Within the time interval Δt_r where $\Delta t_r \gg \Delta t$ [see (19) and (20)] plasma parameters are kept constant, and time averaging is performed. In other words, after every time step Δt the particle weight is added to the score for the cell where it is currently located. Then, the local box-averaged energy density is obtained as a total weight scored in the cell during Δt_r divided by the number of particle steps Δt performed during the time interval Δt_r and by the cell volume. Typically, we use 5×10^5 test particles producing 1.5×10^8 counts per time step. This corresponds to a statistical error of the order of 1% everywhere.

If the fluid element intersects a boundary of the computational region, it is either reflected backwards (with a certain probability) or absorbed. The reflection probability is inferred from the corresponding boundary condition (prescibed heat-flux or temperature). In the present paper, we restrict ourselves to the simplest possible boundary condition, namely to a zero reflection probability for the fluid parcel on all surfaces (limiters, vessel, divertor target). At the inner boundary with the core plasma the heat flux from the core into the edge region is prescribed. This is done by adding a proper amount of particles (heat elements) to the system at each time interval Δt_r Typically, there is no noticeable dependence of the results on the angular distribution of the new particles at the inner boundary.

The method described above is relatively CPU-expensive. We are, essentially, forced to use the MPP (Massively Parallel Processing system) Cray T3E. A procedure inherently well suited for parallelization is a linear Monte Carlo algorithm. Indeed, in the linear case the trajectories are

completely independent. Hence, one can simply distribute the particles among the processing elements. For the nonlinear problem also treated here, this independence prevails only within a time interval Δt_r. Nevertheless, a typical computation has a turn-around time of about an hour with 64 processing elements.

IV. MODELING RESULTS

Various applications of the E3D code have been described elsewhere.[28–30] The beginning of operation of DED at TEXTOR is scheduled for the year 2002. However, many experimental results are available from the 10 years of ergodic divertor campaign at Tore Supra[1] and, most completely, the final review by Ph. Ghendrih given at the 14th PSI Conference in Rosenheim, May 2000, to appear in the proceedings in J. Nucl. Mat. 2001. Many of these experimental and theoretical results (for example, the uniquely structured temperature fields and heat load patterns) are also found in our simulations, which, however, address a geometrically somewhat different configuration. These, therefore, seem to be typical of ergodic divertors in general. In the present paper we will use our tool to study a more fundamental question. We wish at assess, quantitatively, the validity of theoretical models for transport in the ergodic divertor for TEXTOR under far less restrictive geometrical idealizations than necessary for an analytic or semianalytic estimate. The simplifying model assumptions listed below are not restrictions forced by the numerical code but are made to isolate the physics relevant for the above question from side effects.

A. The DED geometry

Although the formulas in Sec. III are fairly general and allow for the use of toroidal magnetic fields computed numerically, e.g., provided by the DIVA-GOURDON combination,[31] in this study we restrict the analysis to the simple analytical model of the magnetic field introduced in Ref. 33. On one hand, this model preserves most of the main features of the real configuration including unperturbed magnetic surfaces, chains of islands and regions with strong ergodicity, on the other hand, it permits the comparison with the results of analytical theory since the magnetic field has the form of a Fourier series. The discussion of the physical background of this model and its relevance to TEXTOR DED[31] as well as the extensive study of the stochastic properties of the field is given in Ref. 33.

The model of the field corresponds to a cylindrical plasma column with periodic ends. In this case the cylindrical coordinate system can be presented, formally, as a quasi-toroidal one with constant metric coefficient $g_{33}=R_0^2$ where R_0 is the large radius of the torus. The magnetic field is represented as $\mathbf{B}=\mathbf{B}^{(0)}+\mathbf{B}^{(1)}$, where

$$\hat{B}_r^{(0)}=0, \quad \hat{B}_\varphi^{(0)}=B_T, \quad \hat{B}_\theta^{(0)}=\frac{r}{qR_0}B_T, \quad q(r)=q_0\frac{r^2}{r_q^2}, \quad (32)$$

is the equilibrium field with constant parameters B_T, q_0, and r_q. Here, a hat denotes physical components of a vector. The perturbation field is given by

TABLE I. Basic parameter set.

Quantity	Notation	Value
Torus big radius	R_0	175 cm
Internal coil radius	a	53 cm
Toroidal field strength	B_T	2 T
Poloidal scope of perturbation	θ_c	60°
Resonant radius	r_q	43 cm
Resonant safety factor	q_0	3
Main poloidal wave number	m_0	12
Main toroidal wave number	n	4
Perturbation amplitude	ε	0.1
Core plasma radius	r_c	38.5 cm
Wall radius	r_w	49 cm
Perpendicular diffusion coefficient	$D_\perp$	3×10^4 cm^2/s
Plasma density	n_e	10^{13} cm^{-3}
Background plasma temperature	T_{eb}	50 eV
Total heat flux from the core	Q	0.25 MW

$$\mathbf{B}^{(1)}=\nabla\times\hat{\mathbf{e}}_\varphi\hat{A}_\varphi,$$
$$\hat{A}_\varphi(r,\theta,\varphi)=-\sum_{m=m_{\min}}^{m_{\max}}\frac{r}{m}B_m(r)\cos(m\theta-n\varphi), \quad (33)$$

with $\hat{\mathbf{e}}_\varphi=$const being the normalized unit vector along the axis of cylindrical coordinates and

$$B_m(r)=\varepsilon B_T\frac{n}{2\pi}mg_m\left(\frac{r}{a}\right)^{M(m)-1},$$
$$g_m=(-1)^{m_0+m}\frac{1}{m_0M_p}\frac{\sin(m_0-m)\theta_c}{\sinh[(m_0-m)/M_p\pi]}. \quad (34)$$

Following Ref. 33 we use the TEXTOR-like set of parameters given in Table I. The resonant radius r_q corresponds to the main resonance $q_0=3$. In addition, the following magnetic field parameters were used, $M(m)=19(|m|-1)/11+1$, $M_p=20$, $m_{\min}=1$, $m_{\max}=30$. The amplitude of the perturbation ε has been varied in the range $\varepsilon=0-0.15$. If not specified otherwise the value from Table I has been used. In contrast to Ref. 33, the toroidal field spectrum contains only the main harmonic $n=4$. This produces no significant difference in the results but shall greatly simplify cross checking of our results by other, simpler tools.

B. Modeling with E3D

We will discuss the following model (see Table I for specifications):

The computational domain corresponds to the TEXTOR edge plasma region between the wall (vacuum chamber) located at $r=r_w=0.49$ m (neglecting the region in the deep shadow of the DED divertor structure) and the hot ''core'' plasma region. The inner boundary of our computational domain is at $r=r_c=0.385$ m.

The heat flux in electrons from the core plasma Q is fixed at r_c. The case with constant plasma density, $n_e=$const, and zero plasma fluid velocity, $\mathbf{V}=0$, has been considered. The perpendicular heat diffusion coefficient $\chi_\perp$ and, correspondingly, the heat conduction coefficient, $\kappa_{\perp e}$ [see (3)], are assumed constant. The classical parallel thermal

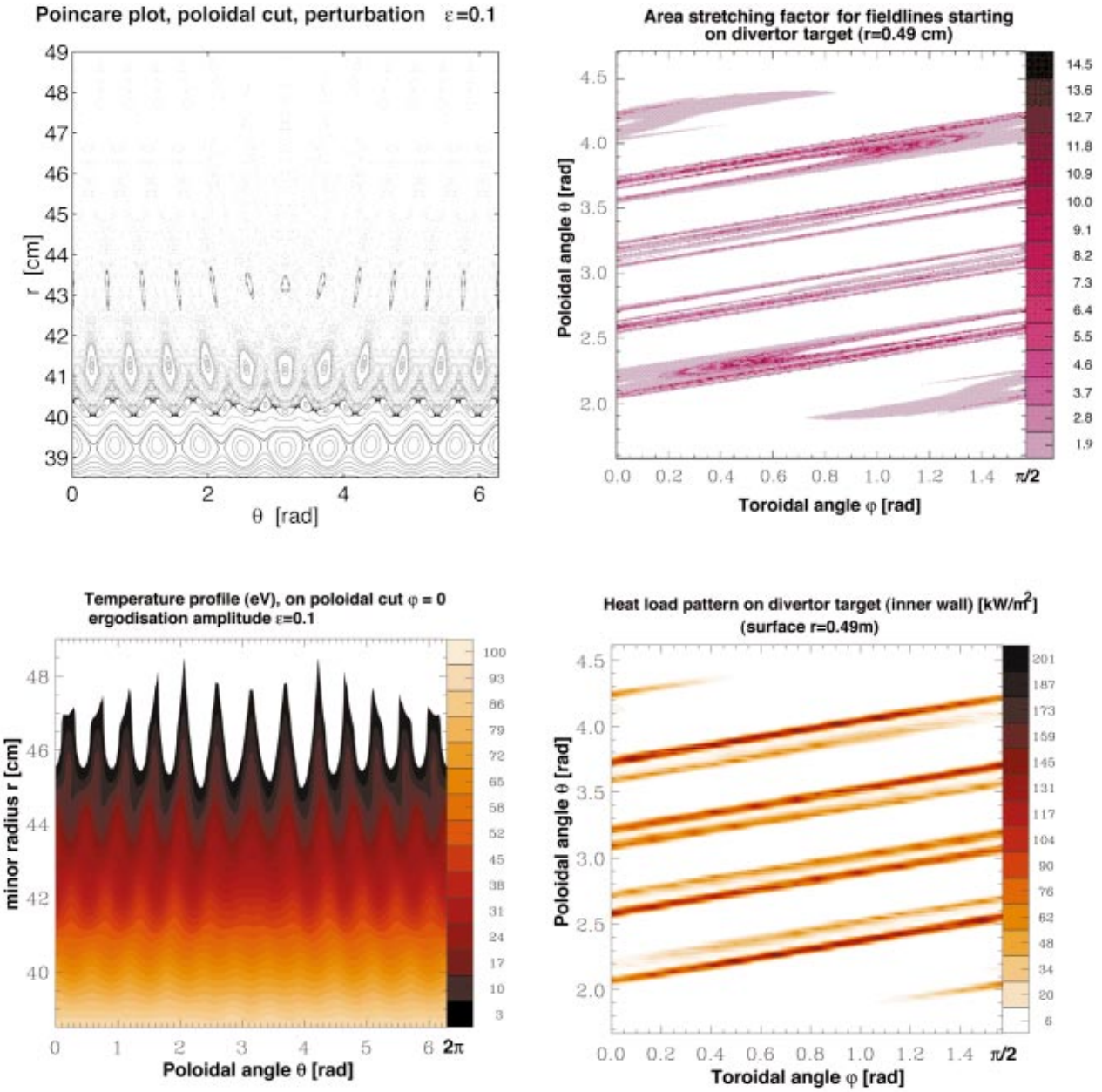

FIG. 4. (Color) Results of the E3D modeling and field line mapping for basic parameter set. (a) Poincaré sections of perturbed field lines at the plane $\varphi = 0$; (b) Decimal logarithm of the ''area stretching factor'' $\sqrt{\mu}$ as a function of the starting position of the field line on the wall ($\sqrt{\mu}$ corresponds to the stretching of the area at the end point of the field line on the wall as compared to the area at the initial point); (c) temperature distribution at the plane $\varphi = 0$; (d) heat flux density at the wall, kW/m^2.

conductivity coefficient[32] used in the computation is a function of the electron temperature, $\kappa_{\|e} = \kappa_{\|e}(T_e)$, and, therefore, the general heat balance problem is nonlinear. In order to separate the purely geometrical effects, in most cases we assumed that $\kappa_{\|e}$ is constant corresponding to the fixed ''background'' plasma temperature $T_e = T_{eb}$. For the same reason, the simplest boundary condition (purely heat absorbing wall) at the vacuum boundary has been used. The basic results of E3D modeling and field line tracing are shown in Fig. 4. It is easy to verify a strong modulation of the temperature field [Fig. 4(c)] by the structure of the magnetic field [compare to Poincaré map Fig. 4(a)]. This corresponds to the effect of a component of fast parallel transport in the radial direction. Similar temperature patterns have been obtained from modeling of the electron heat balance in the ergodic divertor of Tore–Supra.[19,20] As a result, the heat load to the divertor target, i.e., to the inner wall of the torus [see Fig. 4(d)] becomes localized in quite narrow stripes. This seems to be, on first sight, in qualitative agreement with predictions of strongly simplified models for transport in the laminar zone of DED.[16]

However, this is a coincidence, as can be confirmed by inspecting the geometric origin of the main divertor target heat load. This is illustrated by Fig. 4(b) where the ''area

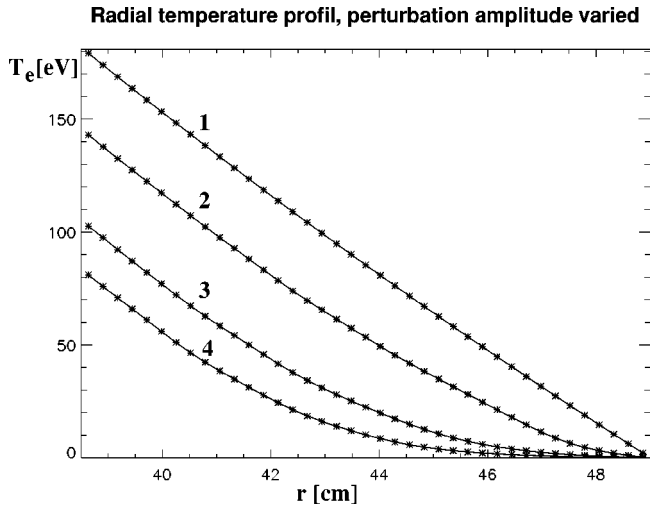

FIG. 5. Angle-averaged radial plasma temperature profile $\langle T_e \rangle$ for various values of perturbation amplitude ε. Curve 1—analytical solution ($\varepsilon=0$), curve 2—$\varepsilon=0.05$, curve 3—$\varepsilon=0.1$, curve 4—$\varepsilon=0.15$.

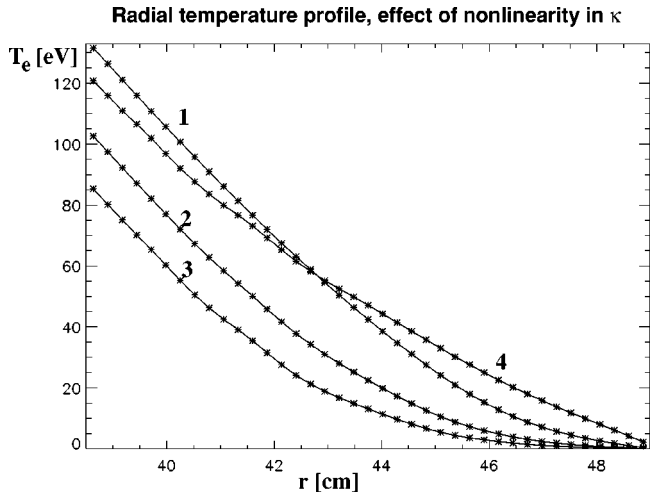

FIG. 6. Angle-averaged (radial) plasma temperature profile $\langle T_e \rangle$, comparison of linear and nonlinear heat diffusion model, for various values of background plasma temperature T_{eb}. Curve 1—$T_{eb}=25$ eV, curve 2—$T_{eb}=50$ eV, curve 3—$T_{eb}=75$ eV, curve 4—''nonlinear'' case. Other parameters are given in Table I.

stretching factor'' $\sqrt{\mu}$ (see Appendix B) is plotted as a function of initial field line position on the divertor target. For the field lines with large connection length L_c this coefficient approaches $\sqrt{\mu}\approx\exp(L_c/L_K)$ where L_K is a Kolmogorov length. One can see that the position of regions with the main heat load correlates with regions where $\sqrt{\mu}>30$. Therefore, high heat load regions are magnetically connected directly to the ergodic zone and do not even belong to the isolated laminar zone studied by Eich *et al.*[16] Also these results from the E3D runs, although for a different configuration, agree qualitatively with experimental and theoretical findings from Tore Supra (loc.cit.).

Although the results above demonstrate a pronounced three dimensional nature of transport in the ergodic divertor, it is interesting to estimate the overall effect of the ergodic divertor on radial heat transport—the ''net radial effect'' of the perturbation, which is depicted in Figs. 5 and 6. In these figures the radial dependencies of the temperature averaged over the poloidal and toroidal angles, $\langle T_e \rangle$, are shown for typical values of the perturbation amplitude, $\varepsilon=0.05-0.15$ and the background plasma temperature, $T_{eb}=25-75$ eV, respectively. The analytical solution there corresponds to the case without perturbation field, $\varepsilon=0$. As one expects, the increase of the perturbation leads to a decrease of the temperature at the edge due to the increased effect of the fast parallel transport on radial profiles. This effect is less pronounced in the ''nonlinear'' case, when the self-consistent value of the background plasma temperature, $T_{eb}=T_e$, is used in the parallel thermal conductivity coefficient $\kappa_{\|e}$. This is due to the fact that in the outer region, in which the perturbed field is the strongest, the parallel thermal conductivity is strongly reduced because of the lower temperature there, ($\kappa_{\|e}\sim T_e^{5/2}$). In order to estimate the influence of the (inclined) parallel transport on temperature profiles, it is interesting to calculate the contribution of the parallel thermal conductivity to the total radial heat flux under quite realistic conditions (e.g., in the presence of walls, limiters, etc. . . .)

A separation of the contributions from the parallel and perpendicular heat transport to the total radial heat flux can naturally be done within the Monte Carlo procedure described in Sec. III as follows. The total radial flux of energy can be evaluated as

$$Q=\frac{w}{\Delta t_r}(N^+-N^-), \tag{35}$$

where N^+ and N^- are the numbers of heat elements crossing the surface $r=$const during the time increment Δt_r in positive (with increasing r) and negative directions, respectively, and w is the energy assigned to a single fluid element, see Sec. III A. Since the ''perpendicular'' and parallel steps entering (18) are performed subsequently, one can write

$$N^{\pm}=N_{\|}^{\pm}+N_{\perp}^{\pm}. \tag{36}$$

$N_{\|}^{\pm}$ and $N_{\perp}^{\pm}$ are the numbers of fluid elements that cross the surface $r=$const after the parallel or perpendicular step, respectively. Thus we obtain the contributions to the total radial energy flux from the classical parallel and anomalous perpendicular diffusion as

$$Q_{\|,\perp}=\frac{w}{\Delta t_r}(N_{\|,\perp}^{+}-N_{\|,\perp}^{-}). \tag{37}$$

In the case of a stationary energy distribution the total flux $Q=Q_{\|}+Q_{\perp}$ is constant (independent of radius, due to our neglect of external sources and sinks), and is equal to the incoming heat flux from the core plasma. If this state is reached in the computation the time interval Δt_r can be taken even longer in order to reduce the statistical error in the computed fluxes further.

The results of simulations of the parallel component of the total radial heat flux, $Q_{\|}$, are presented in Figs. 7 and 8 with dashed lines. Note that $Q_{\|}$ does not exceed the value of the total radial heat flux $Q=0.25$ MW. It approaches this value in the region near the wall where it dominates over $Q_{\perp}$, the contribution of the anomalous perpendicular heat

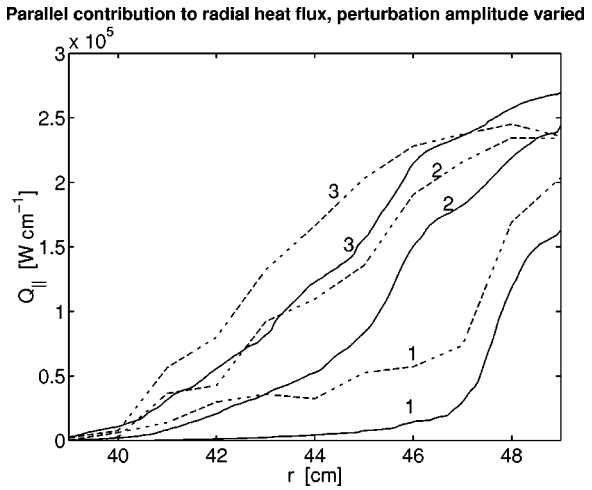

FIG. 7. Parallel component of the total radial heat flux, $Q_{\|}$, for various values of perturbation amplitude ε. Dashed—results of Monte Carlo computation, solid—results of the ''laminar'' model. Curves 1—$\varepsilon=0.05$, curves 2—$\varepsilon=0.1$, curves 3—$\varepsilon=0.15$.

transport to the total radial heat flux. This is typical for a laminar flow established near the wall, by the energy sink action of our walls. We conclude from this that in more realistic studies, in which the sink action may also be caused by the presence of neutral atoms and molecules, purely geometrical arguments to identify laminar flow regions may be grossly in error.

C. Mechanisms of perturbation-induced transport

Let us consider two possible mechanisms of perturbation-induced transport. The first effect comes from the ''diversion'' of field lines which, in particular, takes place in the scrapeoff layer of the usual tokamak divertor and leads to the extension of the radial region containing field lines which directly contact the wall. This provides an effective heat sink due to fast parallel transport along those field lines. In our case this mechanism causes the (often undesired) peaking of the power load onto the target [see Fig. 4(d)], i.e., the perturbation field has a negative side effect in the static regime of DED. The second mechanism is due to the ''braiding'' of the field lines that causes the increase of transport due to the combined effect of fast parallel transport and slow perpendicular transport which de-correlates the electron positions from the field lines.[8,9] The fact that the field lines in the considered region of space end up on the wall is not important here. This case is particularly interesting from the point of view of an ergodic divertor.

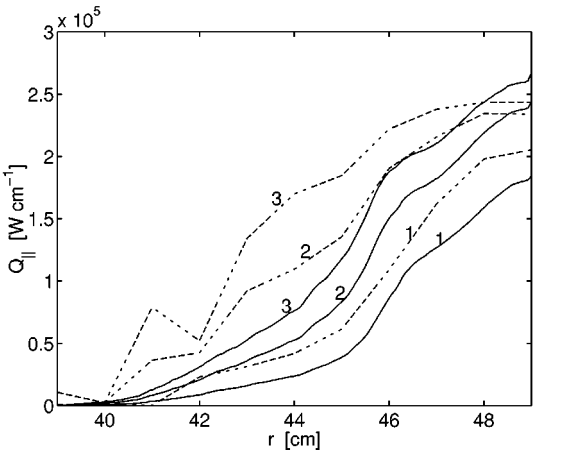

FIG. 8. Parallel component of the total radial heat flux, $Q_{\|}$, for various values of background plasma temperature T_{eb}. Dashed—results of Monte Carlo computation, solid—results of the ''laminar'' model. Curves 1—$T_{eb}=25$ eV, curves 2—$T_{eb}=50$ eV, curves 3—$T_{eb}=75$ eV.

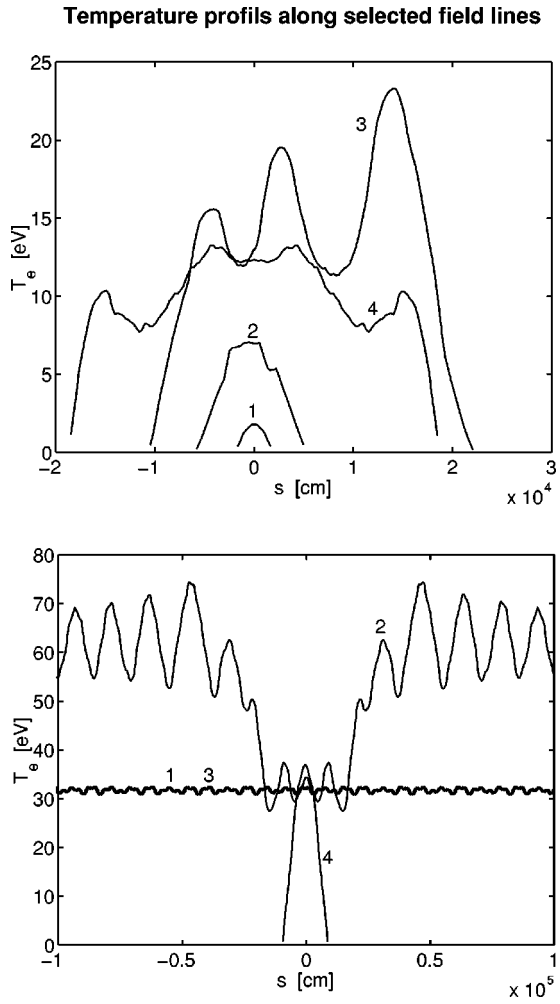

FIG. 9. T_e as a function of the distance along the magnetic-field line s. Field lines intersect the cross-section $\varphi=0$ at $s=0$ and various values of the small radius r: (a) $r=0.46$ cm, (b) $r=0.43$ cm, and poloidal angle θ: curves 1—$\theta=0$, curves 2—$\theta=\pi/4$, curves 3—$\theta=\pi/2$, curves 4—$\theta=\pi$.

Qualitatively the roles of ''diversion-induced'' and ''ergodization-induced'' radial transport in formation of the temperature distribution can be seen from Fig. 9. At the outer regions of the plasma the temperature variation with the distance along the field line fits better to the first mechanism—T_e generally increases from the wall towards the midpoint (stagnation point) of the field line. At the same time, the temperature oscillates along the long field lines, which is more characteristic to stochastic parallel transport (and, notably, again experimentally observed in Tore Supra, see references given above). The dominance of the diversion mechanism at the outer region can be seen also from Fig. 10

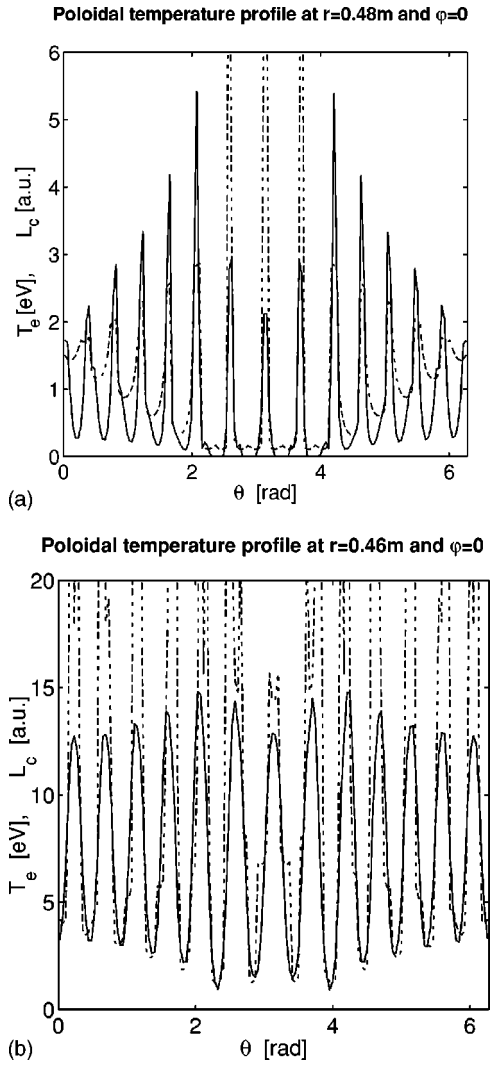

FIG. 10. Plasma temperature T_e (solid) and the connection length L_c (dashed) vs the poloidal angle θ at the cross-section $\varphi=0$. (a) $r=48$ cm; (b) $r=46$ cm.

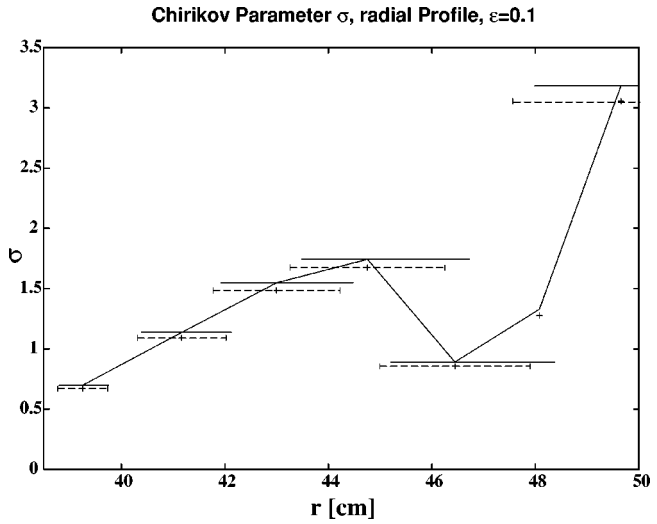

FIG. 11. Chirikov parameter σ vs r for $\varepsilon=0.1$. Island widths are shown with error bars. Dashed bars correspond to the approximate estimate given in the text, solid bars correspond to width (Ref. 36).

where the strong correlation of T_e and the connection length L_c arises at the outer plasma region.

In order to identify the additional radial transport mechanism in more physical terms we consider two simplified transport models that correspond to opposite limiting cases. These are the Rechester–Rosenbluth diffusion model[8,9] describing the effect of braiding and a ''laminar'' sink model which describes the diversion effect. The latter model is based upon the same concepts as the models described in Refs. 14–16. The comparison of the result of the Monte Carlo computation of $Q_\parallel$ with the results of these models will be used to identify the dominant mechanism of perturbation-induced transport.

First, let us estimate the overall radial heat diffusion coefficient due to parallel transport $D_r^{(\parallel)}$ from the known radial profile of the angle-averaged temperature, $\langle T_e\rangle$, and the total parallel heat flux, $Q_\parallel$, using the assumption that radial transport is diffusive. Since $\langle T_e\rangle$ is monotonous and $Q_\parallel$ is positive we obtain a positive ''effective'' diffusion coefficient as

$$D_r^{(\parallel)}=\frac{2Q_\parallel}{3n_e}\left(\frac{\mathrm{d}\langle T_e\rangle}{\mathrm{d}r}\right)^{-1}. \tag{38}$$

Let us compare this quantity with the Rechester–Rosenbluth (RR) diffusion coefficient

$$D_r^{(RR)}=D_{st}D_{\parallel e}\left[L_K\ln\left(\frac{1}{rk_\theta}\left(\frac{D_{\parallel e}}{D_\perp}\right)^{1/2}\right)\right]^{-1}, \tag{39}$$

where D_{st} is the field line diffusion coefficient, $k_\theta=m/r$ is the characteristic perpendicular wave number and L_K is the Kolmogorov length. One should note that for the TEXTOR DED configuration the magnetic field is only very poorly described in terms of field line diffusion. This is because the islands corresponding to main resonances have widths comparable with the size of the scrape-off layer itself.[34] This can be seen also from Fig. 11 where the radial dependence of the Chirikov parameter $\sigma=(\delta_{m+1}+\delta_m)sk_\theta$ and the island widths $\delta_m=2(8qR_0B_m/(sk_\theta B_0))^{1/2}$ corresponding to the magnetic-field model used here are shown. Nevertheless, for rough estimates we use for D_{st} and L_K the results of quasi-linear theory[1,12,13]

$$D_{st}=\pi qR_0\left|\frac{B_m}{B_0}\right|^2,\quad L_K=\frac{qR_0}{4\pi^{1/3}}\left(qR_0k_\theta s\left|\frac{B_m}{B_0}\right|\right)^{-2/3}. \tag{40}$$

Here $s=rdq/(qdr)$ is a shear parameter, B_m is given by (34) and m is the poloidal wave number closest to the resonance, $m=[nq(r)]$.

The results of analytical estimates of the Rechester–Rosenbluth heat diffusion coefficient and ''effective'' diffusion coefficient (38) are shown in Fig. 12. One can see that $D_r^{(\mathrm{RR})}$ becomes compatible with $D_r^{(\parallel)}$ only in the inner region of the considered plasma volume. In this region both $D_r^{(\mathrm{RR})}$ and $D_r^{(\parallel)}$ follow the same scaling with perturbation amplitude and background plasma temperature. On the other hand, the value of the Rechester–Rosenbluth coefficient is quite small compared to the ''intrinsic'' anomalous perpendicular diffusion coefficient $D_\perp$ chosen here.

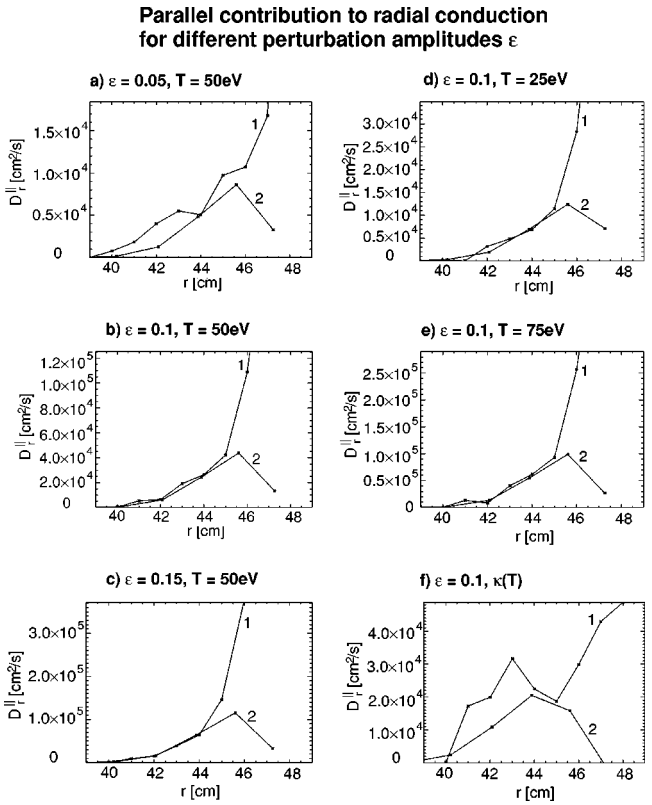

FIG. 12. Overall radial heat diffusion coefficient due parallel transport, $D_r^{(\parallel)}$, vs r for various values of pertubation amplitude, (a) $\varepsilon=0.05$, (b) $\varepsilon=0.1$, (c) $\varepsilon=0.15$, and various values of the background plasma temperature, (d) $T_{eb}=25$ eV (e) $T_{eb}=75$ eV, (f) ''nonlinear case.'' Curve 1—Eq. (38); curve 2—Rechester–Rosenbluth model.

The second limiting case of completely laminar heat flow due to parallel transport along the field lines connected to the wall can be described by a simplified ''sink'' model which uses the self-consistent temperature profile calculated by the Monte Carlo code. Assuming that the heat sink along such selected field lines is the only relevant mechanism we rewrite the 3D problem as a finite set of one-dimensional problems for separate field lines. Each field line starts and ends on a wall surface. They interact with each other by means of an effective heat source.[14] Assuming that the modulus of the magnetic field is constant along the field lines we can present the stationary heat conduction equation in the form

$$\kappa_{\parallel e}\frac{\mathrm{d}^2T_e}{\mathrm{d}s^2}+S_\perp=0, \tag{41}$$

where s is a distance along the field lines and $S_\perp$ is a source term which contains the divergence of the perpendicular flux. Let us consider the toroidal cut $\varphi=0$ with given temperature distribution and distribution of the connection length of the field lines starting from this cut both in the positive and negative toroidal directions, L_c^+ and L_c^-, respectively. Assuming that $S_\perp$ is localized in the midpoint of the field line we find that the parallel temperature gradient is constant along the field line between the midpoint and endpoints on the wall and its modulus is equal to T_e/L_c where L_c is the smallest of L_c^+ and L_c^-. Making use of the fact that the magnetic field is mainly in the toroidal direction we obtain for the toroidal component of the parallel heat flux density

$$q_\varphi(r,\theta)=\pm\kappa_{\parallel e}\frac{T_e(r,\theta)}{L_c(r,\theta)}, \tag{42}$$

where the sign corresponds to the index of the shortest of L_c^+ and L_c^-. Field lines that never intersect the section $\varphi=0$ are located only in small vicinity of the wall (private flux zone). Therefore, the whole area of the surface $r=$const is mapped along the field lines to the section $\varphi=0$ for r not very close to the wall radius r_w. Using the conservation of the parallel flux in the magnetic flux tubes we can express the flux through $r=$const as an integral from the flux density through the toroidal cut $\varphi=0$,

$$Q_\parallel(r)=2\kappa_{\parallel e}\int_{r_c}^{r_w}\mathrm{d}r'r'\int_{-\pi}^{\pi}\mathrm{d}\theta\frac{T_e(r',\theta)\Theta(r-r_{\mathrm{mid}}(r',\theta))}{L_c(r',\theta)N_t(r',\theta;r)}. \tag{43}$$

Here r_c is the core plasma radius, $r_{\mathrm{mid}}(r',\theta)$ is the midpoint radius of the field line passing through $\varphi=0$ at the point (r',θ), $\Theta(x)$ is a Heaviside step function and $N_t(r',\theta;r)$ is the number of crossings of field lines through the toroidal cut. Hence: The factor $1/N_t$ prevents multiple counting of the same field line during the integration. The step function in (43) takes into account the fact that only field lines whose midpoint's radius, r_{mid}, satisfies the condition $r_{\mathrm{mid}}<r$ contribute to the radial flux $Q_\parallel(r)$.

Such a model helps to estimate the parallel transport in the laminar zone, or, more precisely, to identify the parallel transport mechanism due to the magnetic field line diversion. For the parallel radial transport which has a stochastic nature, namely Rechester–Rosenbluth transport, it should give a radial flux which is close to zero. Indeed, in the case of Rechester–Rosenbluth transport the parallel gradient is an alternating function of the distance along the field line s. The parallel transport needs a small amount of perpendicular transport in order to produce a net radial flux. Therefore, in the regions where the stochastic transport dominates, our laminar model would give a very small $Q_\parallel$ due to the large L_c values. Moreover, it obviously gives $Q_\parallel=0$ for the isolated ergodic layer.

The comparison of the results of this model and of the 3D calculation for different perturbation field amplitudes ε and background plasma temperatures T_{eb} (Figs. 7 and 8) confirms that the diversion mechanism is dominant in the outer plasma region. At the same time the laminar model gives smaller contribution in the central part of the considered region where the ''ergodization'' mechanism takes over.

We see that neither a laminar flow model nor an ergodic transport model can describe the entire scrape-off layer (SOL) of an ergodic divertors properly. We have seen that the consideration of the mutual influence of the regions with quite distinct transport physics is essential for any attempt to quantitative transport modeling for ergodic divertors.

V. CONCLUSION

A new Monte Carlo tool for modeling three-dimensional edge plasmas of toroidal confinement devices has been developed and realized in the 3D Monte Carlo code E3D. It extends other 3D CFD (computational fluid dynamic) projects in fusion edge plasma physics in that it enables one to account, explicitly, for the presence of subregions of ergodic force fields (here: The magnetic field), consistently linked to other domains of a more laminar flow character. The code is based upon multiple magnetic coordinate systems linked by an ''interpolated cell mapping.'' This approach has been applied to parameters typical for the dynamic ergodic divertor of the tokamak TEXTOR-94. The computations have been performed both with fixed parallel thermal conductivity and self-consistently accounting for their nonlinear dependence on the temperature. The computations in the first case had the primary purpose to study the effects of the magnetic-field topology on the heat transport rather than other effects. In order to determine the additional heat flux caused by the effect of the magnetic-field perturbation, the radial heat fluxes due to the classical parallel and anomalous perpendicular diffusion could be separated, a special feature of the microscopic Monte Carlo procedure. The additional heat flux originating from the radial transport along the magnetic-field lines is shown to be in agreement with the results of the Rechester–Rosenbluth diffusion model in the inner region of the TEXTOR DED plasma. Therefore the additional transport in this region can be attributed to the magnetic field line braiding. This additional transport appears to be small compared to the effect of the anomalous perpendicular diffusion. In a much wider region in the neighborhood of the wall, however, a simple model based upon parallel transport on inclined field lines contacting the wall provides a better qualitative agreement with results of the Monte Carlo computation of the additional heat flux. This model describes the effect of the magnetic field line diversion—the same structure as in the scrape-off layer of more common poloidal divertor concepts, except for the breaking of symmetry between plasma and recycling flow.

ACKNOWLEDGMENTS

Authors are very grateful to Ph. Ghendrih (CE Cadarache) for many most useful discussions and suggestions. They also wish to thank S. Abdullaev (FZ-Jülich) for providing the model magnetic field for the TEXTOR-DED configuration.

One of us, S.V.K, gratefully acknowledges the financial support from the Technical University Graz (Austria) and the hospitality of the Institut für Theoretische Physik during scientific visits to Graz. This work was partly supported by the Association EURATOM-OEAW under Contract No. ERB 5004 CT 96 0020 and by the BMWV (Österreichisches Bundesministerium für Wissenschaft und Verkehr) under Contract No. GZ 4229/1-III/A/5/99.

APPENDIX A: ERROR INDUCED BY SPLINING

The error of the splining procedure used for reconstruction of the magnetic field mapping function $X^1_{\pm,m} \sim h^r L_\parallel$ can be estimated using the residual term of the bicubic spline as

$$\delta r \sim X^1_{\pm,m}\left(\frac{h}{L_\perp}\right)^4 \sim \left(\frac{h}{L_\perp}\right)^4 h^r L_\parallel . \tag{A1}$$

Here h^r is the radial component of the unit vector along the magnetic field, $L_\parallel$ is the characteristic distance between the reference cuts along the magnetic field line, $L_\perp$ is the characteristic perpendicular scale of the perturbed magnetic field and h is the size of the mesh interval. First, we assume the worst case when the errors add up with the same sign each time the coordinate change between the local coordinate systems is performed. The coordinate change occurs, on average, once per time interval $\delta t \sim L_\parallel^2/\chi_{\parallel\alpha}$ where $\chi_{\parallel\alpha}$ is the parallel heat diffusion coefficient (3). Then, the error will induce an artificial perpendicular convection with velocity $V_{\mathrm{art}} = \delta r/\delta t$. This velocity must be kept well below the real perpendicular fluid velocity coming from the perpendicular diffusion

$$V_\perp = D_\perp \left|\frac{\nabla u}{u}\right| \sim \frac{D_\perp}{a}, \tag{A2}$$

where $D_\perp$ is a perpendicular diffusion coefficient and a is a characteristic perpendicular scale of the temperature (plasma small radius in the worst case). Thus for the allowed systematic error (A1) we get the limitation

$$|\delta r| \ll \frac{D_\perp L_\parallel^2}{\chi_{\parallel\alpha}\, a}. \tag{A3}$$

If the errors add up with a random sign, which is much more likely, the splining error will result in an artificial cross-field diffusion with coefficient $D_{\mathrm{art}} \sim \delta r^2/\delta t$. This diffusion coefficient must be smaller than $D_\perp$. This means a weaker limitation on δr than (A3),

$$|\delta r| \ll \left(\frac{D_\perp}{\chi_{\parallel\alpha}}\right)^{1/2} L_\parallel . \tag{A4}$$

The parameters of the ''magnetic mesh'' described in Sec. III C were chosen to satisfy the ''worst case'' condition (A3).

APPENDIX B: CALCULATION OF THE CONNECTION LENGTH AND LYAPUNOV EXPONENTS

In order to introduce the cell mapping procedure for calculation of the connection length and of Lyapunov exponents we use a conventional method for calculation of the Lyapunov exponent from a given vector field (see, e.g., Ref. 35). The magnetic-field line equations with toroidal angle φ as an integration variable are

$$\frac{\mathrm{d}}{\mathrm{d}\varphi} y^i = f^i(\mathbf{y},\varphi), \quad i=1,2, \quad \frac{\mathrm{d}s}{\mathrm{d}\varphi} = \frac{1}{h^\varphi}, \tag{B1}$$

where $f^i = h^i/h^\varphi$ is a vector field, $\mathbf{y} \equiv (y^1, y^2) = (r,\theta)$ and s is the distance along the field line. The flow induced by this

vector field is the solution to this set of equations for any initial point y_0^i (some general curvilinear coordinates, quasi-toroidal in our case)

$$y^i = Y^i(\mathbf{y}_0, \varphi_0; \varphi), \frac{\partial}{\partial \varphi} Y^i(\mathbf{y}_0, \varphi_0; \varphi)$$

$$= f^i(\mathbf{Y}(\mathbf{y}_0, \varphi_0; \varphi), \varphi), \quad Y^i(\mathbf{y}_0, \varphi_0; \varphi_0) = y_0^i. \tag{B2}$$

The separation δy^i of a neighboring field line evolves according to

$$\delta y^i = \frac{\partial Y^i}{\partial y_0^j} \delta y_0^j \equiv M_j^i(\mathbf{y}_0, \varphi_0; \varphi)\ \delta y_0^j, \tag{B3}$$

where $M_j^i \equiv \partial Y^i / \partial y_0^j$ is the deformation tensor of the flow field. The evolution of this tensor along the field line is

$$\frac{\partial}{\partial \varphi} M_j^i(\mathbf{y}_0, \varphi_0; \varphi) = \left. \frac{\partial f^i(\mathbf{y})}{\partial y^k} \right|_{\mathbf{y} = \mathbf{Y}(\mathbf{x}_0, \varphi_0; \varphi)} M_j^k(\mathbf{y}_0, \varphi_0; \varphi), \tag{B4}$$

$$M_j^i(0, \mathbf{y}_0) = \delta_j^i. \tag{B5}$$

The deformation tensor has the property

$$M_j^i(\mathbf{y}_0, \varphi_0; \varphi) = M_k^i(\mathbf{Y}(\mathbf{y}_0, \varphi_0; \varphi_1), \varphi_1; \varphi) M_j^k(\mathbf{y}_0, \varphi_0; \varphi_1). \tag{B6}$$

The change in length of the displacement will be

$$|\delta \mathbf{r}|^2 = \delta y^i g_{ij} \delta y^j = \delta y_0^k M_k^i g_{ij} M_l^j \delta y_0^l = \delta y_0^k G_{kl} \delta y_0^l,$$
$$G_{kl} \equiv M_k^i g_{ij} M_l^j, \tag{B7}$$

where $\delta \mathbf{r} = \mathbf{r}(\mathbf{y} + \delta \mathbf{y}, \varphi) - \mathbf{r}(\mathbf{y}, \varphi)$, and $\mathbf{r}(\mathbf{y}, \varphi)$ is the radius-vector of the point with curvilinear coordinates $\mathbf{y}, \varphi$. Here g_{ij} is the covariant metric tensor of the quasi-toroidal coordinates in the endpoint of the trajectory (note that only the components with $i, j = 1,2$ are used). Let us write an eigenvector equation in the form

$$g_{(0)}^{mk} G_{kl}\ \delta y_0^l = \mu\ \delta y_0^m, \tag{B8}$$

where $g_{(0)}^{ij}$ is the contravariant metric tensor in the starting point of the trajectory and choose the eigenvector with the largest eigenvalue. (Both matrices G_{kl} and $g_{(0)}^{mk}$ on the left-hand-side (lhs) are symmetric and positive definite, and, therefore, eigenvalues μ are real and positive.) We can define the respective Lyapunov exponent as

$$\lambda(\delta \mathbf{y}_0, \mathbf{y}_0, \varphi_0) = \frac{1}{L_k} = \lim_{s \to \infty} \frac{1}{s} \log \frac{|\delta \mathbf{r}|}{|\delta \mathbf{r}_0|} = \lim_{s \to \infty} \frac{\log \sqrt{\mu}}{s}, \tag{B9}$$

where $\delta \mathbf{r}_0 = \mathbf{r}(\mathbf{y}_0 + \delta \mathbf{y}_0, \varphi_0) - \mathbf{r}(\mathbf{y}_0, \varphi_0)$ is the initial displacement with the length

$$|\delta \mathbf{r}_0|^2 = \delta y_0^i g_{ij}^{(0)} \delta y_0^j, \tag{B10}$$

and $\delta \mathbf{y}_0$ is the eigenvector corresponding to the eigenvalue μ of the eigenvalue problem (B8). The geometrical meaning of $\sqrt{\mu}$ is the following. At an initial point of the field line (on the wall) in a plain $\varphi = \text{const}$ we introduce an (infinitesimal) small area which has a shape of a circle with radius r_0. The boundary of this area and its center point are traced along the field lines until the center hits the wall another time. Then the circular boundary is transformed to an ellipse with large semiaxis a and approximately the same area as the initial circle. The ratio a/r_0 is the stretching factor $\sqrt{\mu}$.

In a truly chaotic system, the Lyapunov exponential becomes independent of the starting point $\mathbf{y}_0, \varphi_0$ of the chosen trajectory, for sufficiently large times. In a Hamiltonian system the area when moved with the flow is conserved (more precisely, it is inversely proportional to the local value of physical toroidal magnetic field component $\hat{B}_\varphi$) but its shape will be deformed. The maximum elongation is described by the Kolmogorov length L_k which is the inverse of the largest Lyapunov exponent.

One can check that the eigenvalues obtained from (B8) are independent from the choice of variables $\mathbf{y}$. In particular, one can use the canonical action-angle variables $I = r^2/(2R_0^2)$ and θ (see Ref. 33).

During the calculations the position of any field line can be traced with the help of a Poincaré map instead of direct integration of the field line equations. The map $\hat{Y}^i(\mathbf{y})$ is precomputed numerically on the mesh of initial points using the trajectories Y^i,

$$\hat{Y}^i(\mathbf{y}) = Y^i(\mathbf{y}, \varphi_0; \varphi_0 + \Delta\varphi), \tag{B11}$$

where $\Delta\varphi = \pi/2$ is the toroidal period of the field (see Sec. IV A). Then, during the main computation, Poincaré mapping is performed with the help of interpolating map data using bicubic splines. Together with the map, also the deformation tensor $\hat{M}_k^i$ is stored where

$$\hat{M}_k^i(\mathbf{y}) = M_k^i(\mathbf{y}, \varphi_0; \varphi_0 + \Delta\varphi). \tag{B12}$$

Using the group property of the deformation tensor (B6), it can be also obtained by successive maps

$$M_k^i(\mathbf{y}, \varphi_0; \varphi_0 + n\Delta\varphi)$$

$$= \hat{M}_{k_{n-1}}^i(\mathbf{y}_{n-1}) \hat{M}_{k_{n-2}}^{k_{n-1}}(\mathbf{y}_{n-2}) \cdots \hat{M}_{k_1}^{k_2}(\mathbf{y}_1) \hat{M}_k^{k_1}(\mathbf{y}), \tag{B13}$$

where $\mathbf{y}_k$ is the field line footprint after k Poincaré mappings

$$y_k^i = \hat{Y}^i(\mathbf{y}_{k-1}). \tag{B14}$$

If, after a certain number of mappings, the field line hits the wall within the magnetic-field period, connection length s and deformation tensor are obtained by direct integration of the field line equation (B1) and the corresponding equations for the deformation tensor (B4) with initial conditions on the Poincaré cut given by the last successful mapping.

Such a procedure allows a fast evaluation of the connection and Kolmogorov lengths for relatively complex magnetic fields, in particular, produced by real coils and calculated with the help of the Biot–Savart law. At the same time, e.g., for the twist map the deformation tensor $\hat{M}_k^i$ can be obtained analytically.[33]

[1] Ph. Ghendrih, A. Grossman, and H. Capes, Plasma Phys. Controlled Fusion **38**, 1653 (1996).
[2] W. D. D'haeseleer, W. N. G. Hitchon, J. D. Callen, and J. L. Shohet, *Flux Coordinates and Magnetic Field Structure* (Springer-Verlag, Berlin, 1991).
[3] B. J. Braams, *A Multi-fluid Code for Simulation of the Edge Plasma in*

Tokamaks, NET-Report, EUR-FU/XII-80/87/68 (Commission of the European Communities, Brusseles, 1987).
[4]M. Borchardt, A. Mutzke, J. Nuhrenberg, J. Riemann, R. Schneider, and S. Weber, in *25th EPS Conference on Controlled Fusion and Plasma Physics, Maastricht, 14–18 June 1999, ECA* (European Physical Society, Petit-Lancy, 1999), Vol. 23J, pp. 1501–1504.
[5]Y. Feng, F. Sardei, and J. Kisslinger, J. Nucl. Mat. **241–243**, 930 (1997).
[6]E. Strumberger, Nucl. Fusion **37**, 19 (1997).
[7]E. Strumberger, J. Nucl. Mater. **266–269**, 1207 (1999).
[8]A. B. Rechester and M. N. Rosenbluth, Phys. Rev. Lett. **40**, 38 (1978).
[9]T. H. Stix, Nucl. Fusion **18**, 353 (1978).
[10]A. Samain, H. Capes, Ph. Ghendrih, and F. Nguyen, Phys. Rev. B **5**, 471 (1993).
[11]M. Z. Tokar, Phys. Plasmas **6**, 2808 (1999).
[12]M. N. Rosenbluth, R. Z. Sagdeev, J. B. Taylor, and G. M. Zaslavsky, Nucl. Fusion **6**, 297 (1966).
[13]J. A. Krommes, C. Oberman, and R. G. Kleva, J. Plasma Phys. **30**, 11 (1983).
[14]E. Strumberger, Nucl. Fusion **36**, 891 (1996).
[15]F. Nguyen, Ph. Ghendrih, and A. Grosman, Nucl. Fusion **37**, 743 (1997).
[16]K. H. Finken, T. Eich, and A. Kaleck, Nucl. Fusion **38**, 515 (1998).
[17]G. Fuchs, D. Reiter, and B. Steffen, *Plasma Transport in Ergodized Fields IAEA TECDOC* (International Atomic Energy Agency, Vienna, 1989), p. 536.
[18]P. Beyer, X. Garbet, and Ph. Ghendrih, Phys. Plasmas **5**, 4271 (1998).
[19]M. Becoulet, Ph. Ghendrih, H. Capes, and A. Grossman, in *25th EPS Conference on Controlled Fusion and Plasma Physics, Maastricht, 14–18 June 1999, ECA* (European Physical Society, Petit-Lancy, 1999), Vol. 23J, pp. 989–992.
[20]M. Becoulet, Ph. Ghendrih, H. Capes, and A. Grossman, *Electron Heat Transport in Stochastic Magnetic Layer*, Report EUR-CEA-FC-1667, F-13108 St. Paul-lez-Durance, CEDEX, France, 1999.
[21]H. Wobig and R. H. Fowler, Plasma Phys. Controlled Fusion **30**, 721 (1988).
[22]S. Feron and Ph. Ghendrih, in *24th EPS Conference on Controlled Fusion and Plasma Physics, Berchtesgaden, 9–13 June 1997, ECA* (European Physical Society, Petit-Lancy, 1997), Vol. 21A, pp. 185–187.
[23]B. H. Tongue, Physica D **8**, 401 (1987).
[24]A. Montvai and D. F. Düchs, in *Physics Computing '92, Prague, 1992* (World Scientific, Singapore, 1993), p. 417.
[25]M. de Rover, N. J. Lopes Cardozo, and A. Montvai, Phys. Plasmas **3**, 4478 (1996).
[26]S. V. Kasilov, V. E. Moisenko, and M. F. Heyn, Phys. Plasmas **4**, 2422 (1997).
[27]S. V. Kasilov, W. Kernbichler, V. V. Nemov, and M. F. Heyn, in *25th EPS Conference on Controlled Fusion and Plasma Physics, 29 June–3 July 1998, Prague, Czech Republic, ECA* (European Physical Society, Petit-Lancy, 1998), Vol. 22C, p. 1726.
[28]A. Runov and D. Suender, *Monte Carlo Modelling of the Transport Phenomena in Magnetic Islands*, Report Max-Planck-Institut fuer Plasmaphysik 8/8, Garching bei Muenchen, 1995.
[29]A. M. Runov, D. Reiter, and S. V. Kasilov, in *25th EPS Conference on Controlled Fusion and Plasma Physics, 29 June–3 July 1998, Prague, Czech Republic, ECA* (European Physical Society, Petit-Lancy, 1998), Vol. 22C, p. 1812.
[30]D. Reiter, A. Runov, and S. Kasilov, in *ISPP-19, Theory of Fusion Plasmas*, edited by J. W. Connor, O. Sauter, and E. Sindoni (Editrice Compositori, Bologna, 2000), pp. 185–198.
[31]K. H. Finken, M. Baelmans, P. Boerner *et al.*, Fusion Eng. Des. **37**, 1 (1997).
[32]S. I. Braginskii, in *Reviews of Plasma Physics*, edited by M. A. Leontovich (Consultants Bureau, New York, 1965), Vol. 1, p. 205.
[33]S. S. Abdullaev, K. H. Finken, A. Kaleck, and K. H. Spatschek, Phys. Plasmas **5**, 196 (1998).
[34]Ph. Ghendrih, A. Grossman, and A. Kaleck, in *24th EPS Conference on Controlled Fusion and Plasma Physics, Berchtesgaden, 9–13 June 1997, ECA* (European Physical Society, Petit-Lancy, 1997), Vol. 21A, pp. 1685–1688.
[35]E. Ott, *Chaos in Dynamical Systems* (Cambridge University Press, Cambridge, 1993).
[36]V. F. Aleksin and V. P. Sebko, Nucl. Fusion **8**, 145 (1968).